



Internal tides off the Amazon shelf – Part 2: temperature variability at tidal frequencies

- 4 Fernand Assene^{1,2,3}, Ariane Koch-Larrouy^{1,4}, Carina Regina de Macedo^{1,5,6}, Isabelle Dadou¹,
Michel Tchilibou⁷, Guillaume Morvan¹, Damien Allain¹, Simon Barbot¹, Alex Costa da Silva⁸,
Jérôme Chanut², Vincent Vantrepotte⁵, Florent Lyard¹, Edward Zaron⁹, Trung-Kien Tran⁵
- 8 1. *Université de Toulouse, LEGOS (CNES/CNRS/IRD/UT3), Toulouse, France.*
2. *Mercator Ocean International, 31400 Toulouse, France.*
3. *Department of Maritime Navigation and Information Systems, National Advanced School of Maritime and
Ocean Science and Technology (NASMOST), University of Ebolowa, P.O. Box: 292 Kribi, Cameroon.*
12 4. *CECI CNRS/Cerfacs/IRD, Université de Toulouse, Toulouse, France.*
5. *Univ. Littoral Côte d'Opale, CNRS, Univ. Lille, IRD, UMR 8187 - LOG - Laboratoire d'Océanologie et de
Géosciences, F-62930 Wimereux, France.*
16 6. *Earth Observation and Geoinformatics Division, National Institute for Space Research (INPE), São José
dos Campos, Brazil.*
7. *Collecte Localisation Satellites, 31500 Ramonville Saint-Agne, France.*
8. *Departamento de Oceanografia da Universidade Federal de Pernambuco, DOCEAN/UFPE, Recife, Brazil.*
20 9. *College of Earth, Ocean, and Atmospheric Sciences, Oregon State University, Corvallis, OR, USA.*

Correspondence to: Fernand Assene fernandassene@hotmail.com

24

Abstract

28 The northern Brazilian region constitutes one of the most energetic tidal environments of the tropical Atlantic,
where distinct mixing regimes coexist over short spatial scales. While barotropic tidal motions exert a dominant
control on turbulent mixing across the shallow continental shelf, energy dissipation associated with internal tides
(ITs) governs the intensity and distribution of mixing at the shelf-break and in offshore waters. As demonstrated
32 in the Part 1 companion study (Assene et al., 2024), these contrasting processes strongly influence upper-ocean
thermal structure. Yet, the expression of tidal forcing in temperature variability at tidal timescales—particularly
at semidiurnal (principal solar: M_2 and principal lunar: S_2) and fortnightly (lunisolar synodic: MSf)
frequencies—remains poorly documented in this region. In this study, we investigate the role of tides, with a
focus on ITs, in shaping temperature variability throughout the NBR by combining long-term satellite sea
36 surface temperature (SST) records with high-resolution three-dimensional numerical simulations operated with
and without tidal forcing.

The main findings are as follows:

- 40 a. At semidiurnal frequencies, temperature variability at the sea surface is very weak offshore and remains
modest over the continental shelf, consistent with the prevalence of barotropic mixing that acts largely
as a depth-integrated process in shallow waters. In contrast, pronounced temperature variability



- emerges at thermocline depths, with mean amplitudes reaching approximately 0.6 °C for S_2 and exceeding 2 °C for M_2 . The spatial structure of these subsurface signals aligns closely with simulated mode-1 and mode-2 IT wavelengths, propagation pathways, and dissipation hot-spots, underscoring the central role of ITs in driving semidiurnal thermal variability below the surface mixed layer;
- 44
- b. Fortnightly (MSf) variability contrasts sharply with the semidiurnal response. Both satellite observations (MUR, TMI) and tidal simulations reveal low amplitudes on the order of 0.15 °C, with maximums confined to the northwestern shelf where Spring–Neap modulation of barotropic tidal currents is the dominant tidal process. Composite analyses contrasting Spring versus Neap conditions further suggest that this MSf variability manifests primarily as a net cooling with the same amplitude. At the surface, neither model nor satellite observations exhibit a significant SST expression at MSf frequency along internal tide propagation pathways. This may reflect a rapid atmospheric heat flux adjustment that counteracts internal tide–induced cooling and/or the inherently incoherent nature of IT dynamics that disperses energy across frequencies, preventing harmonic methods from capturing a clear MSf signature. At subsurface depths (~120 m), MSf temperature variability becomes more pronounced along IT pathways, particularly near the shelf break and downstream of generation sites where dissipation is strongest.
- 48
- 52
- 56
- c. The vertical penetration depth of tidally driven temperature variability decreases systematically with increasing tidal period, from penetration depths approaching 2500 m for M_2 , to 800–1000 m for S_2 and 600–800 m for MSf. These contrasts indicate that the capacity of tidal motions to influence the water column depends strongly on the available energy at each frequency and points to a frequency-dependent control of deep-ocean mixing and heat redistribution.
- 60

Together, these findings provide the first regional quantification of temperature variability at tidal frequencies in the northern Brazilian region and demonstrate that internal tides constitute a major driver of subsurface thermal structure across this dynamically energetic margin. This improved characterization is essential for understanding heat redistribution, interpreting coastal and open-ocean temperature variability, and ultimately constraining the representation of tidal processes in ocean and climate models.

64

68

Introduction

High-frequency tidal motions (principal solar: M_2 and principal lunar: S_2) constitute a major contributor to ocean mixing, with energy dissipation from internal tides (ITs) and barotropic tides playing a central role in sustaining vertical exchanges and shaping the thermal structure of the water column (Munk and Wunsch, 1998; Egbert and Ray, 2000; Kouogang et al., 2025). This mixing generates temperature variability at corresponding tidal frequencies, a process well documented in several energetic regions of the global ocean. Most advances to date originate from point-based mooring observations (van Haren and Gostiaux, 2009; van Haren et al., 2016; Purwandana et al., 2021) or from transects acquired using autonomous underwater vehicles (Cazenave et al., 2011; Smith et al., 2016). However, despite the development of modern observing platforms, the production of

72

76



80 regional-scale assessments of high-frequency temperature variability remains limited. Gaps in both spatial and
temporal resolution of in situ and satellite data limit our ability to characterize the spatial structure of
temperature variability at semidiurnal frequencies such as M_2 or S_2 .

84 In addition, an important process further challenges this characterization: ITs are not exclusively expressed as
coherent tidal waves. A significant fraction of IT energy is released as incoherent signals resulting from
scattering, refraction by mesoscale and submesoscale features, and the cumulative effect of multiple generation
sites (Zaron, 2017; Buijsman et al., 2017 and Tchilibou et al., 2022). These incoherent components lose phase
consistency over space and time and are therefore poorly captured by traditional harmonic analysis. As a result,
88 regional atlases of tidally driven thermal variability underestimate or do not resolve this diffused, intermittently
organized component of IT dynamics. The limited capacity of existing observation systems to distinguish
between coherent and incoherent ITs contributes to persistent uncertainty regarding their contribution to
regional-scale temperature variability.

92 Contrasting with high-frequency, valuable progresses have been achieved for lower tidal frequencies associated
with the fortnightly Spring–Neap modulation (lunisolar synodic: MSf, 14.77 days), resulting from the nonlinear
interaction between the M_2 and S_2 semidiurnal constituents (Ray and Susanto, 2016). Thanks to the emergence
of high-resolution daily satellite temperature products and numerical modeling, regional studies have revealed
MSf temperature variability with amplitudes of 0.1 to 0.5 °C in the Indonesian Seas (Ray and Susanto, 2016;
96 Nugroho et al., 2018; Susanto and Ray, 2022) and in Hong Kong coastal waters (Susanto et al., 2019). Although
moderate in magnitude, MSf thermal variability has been shown to influence key atmospheric processes—trade
winds, cloud convection, and the Asian monsoon system (Martinez-Díaz-de-León et al., 2013; Iwasaki et al.,
2015; Susanto et al., 2019; Ray and Susanto, 2019). In contrast, despite its demonstrated importance elsewhere,
100 fortnightly variability in the northern Brazilian region remains understudied, with recent work focusing primarily
on MSf modulation of chlorophyll-a (de Macedo et al., 2025) rather than temperature.

The northern Brazilian region (NBR) stands among the most energetic IT environments of the tropical Atlantic,
characterized by multiple hot-spots of coherent IT generation and dissipation along the shelf break and farther
104 offshore (Magalhaes et al., 2016; Barbot et al., 2021; Tchilibou et al., 2022; Solano et al., 2023; Assene et al.,
2024). Yet, the region is also marked by intense interactions with vigorous mesoscale and submesoscale
circulation, suggesting a substantial fraction of IT energy may propagate as incoherent waves, dispersing and
losing phase lock over basin to sub-basin scales. This mixture of coherent and incoherent tides likely sustains
108 significant thermal variability, but in a manner that is more diffused spatially and temporally, offering an
additional explanation for the absence of clear tidal signatures in low-frequency (e.g., MSf) harmonic analyzes.
Meanwhile, barotropic tides dissipate across the broad continental shelf (Ruault et al., 2020; Assene et al., 2024).
In this region, M_2 and S_2 remain the dominant tidal constituents (Gabioux et al., 2005; Barbot et al., 2021;
112 Fassoni-Andrade et al., 2023), whose close frequencies produce the MSf modulation (Souza and Pineda, 2001;
Ray and Susanto, 2016; Fassoni-Andrade et al., 2023).

In a previous companion study (Assene et al., 2024), we examined the seasonal imprint of tidal forcing using
twin simulations with and without tides. We found that barotropic and ITs jointly induce a surface cooling of
116 approximately 0.3 °C, accompanied by enhanced subsurface cooling above the thermocline (~1.2 °C) and



warming below. These changes were primarily driven by vertical mixing, whereas advective processes played a secondary role below the mixed layer. Yet, despite their significant seasonal impact, the spatial structure of temperature variability specifically at tidal frequencies, and the respective contributions of coherent and incoherent internal tides, remain uncharacterized in the northern Brazilian region.

The present study aims to fill this gap by quantifying temperature variability at the two dominant semidiurnal tidal frequencies and at the fortnightly frequency associated with their nonlinear interaction, and by documenting the spatial imprint of coherent ITs contributions. To achieve this, we combine satellite SST records with high-resolution numerical simulations able to resolve barotropic tides, coherent ITs.

This paper is structured as follows. Section 2 describes the satellite products, the model configuration, and the analysis methods. Section 3 presents the results, section 4 discusses their implications, and section 5 outlines conclusions and perspectives.

128

2. Data and Methods

2.1. Data

We used 10-year daily temperature datasets, from January 2007 to December 2016, combining two observational SST products and simulated temperatures. In addition, we used the simulated hourly temperature over the year 2015, which are the most recent hourly data produced with the model. Note that the simulated temperatures come from the tidal and non-tidal simulations described above.

2.1.1. Remote sensing of SST

SST observations include microwave measurements with low spatial resolution and infrared measurements from the GHRSSST product with finer resolution.

- TMI SST

Microwave satellites obtain measurements through clouds and are therefore very useful in areas with high cloud cover throughout the year, such as the NBR. TMI SST comes from the Tropical Rainfall Measurement Mission (TRMM), which provides SST using the TRMM Microwave Imager. We used the latest version of this product (v7.1) which contains daily SST data at $\frac{1}{4}^\circ$ horizontal resolution (~ 25 km). This low resolution requires a mask of 50–75 km around coastline, owing to the microwave sensor footprint and the possible land contamination (Chelton and Wentz 2005). For a full description of this product, see Wentz (2015).

- MUR SST

The latest version of Multi-scale Ultra-high-Resolution SST (MUR SST v4.1) product is used here. It is a daily set of SST estimates on a global $0.01^\circ \times 0.01^\circ$ grid resolution (~ 1 km). SST fields are made up of the merging of four satellite data types (High-resolution Infrared, AVHRR Infra-red, Microwave and Ice fraction) from 14 satellite missions, and *in situ* data. Infrared measurements cannot penetrate clouds, which are highly present in our region during the year. Then these measurements are merged with Microwaves measurements to avoid this limitation. A meshless multiscale interpolation method performs weighted least-squares optimization. The MUR SST outputs are produced from different temporal (1–10 days) and spatial (1–10 km) resolution temperature



156 inputs. The interpolation of various measurements on a daily restructured grid reduces gaps in data compared with using a single type of satellite measurement (see Ray and Susanto, 2016), and ultimately, to reduce or even avoid errors in the analyzed results (e.g., Yang et al., 2021). The full description of MUR SST data is given by Chin et al. (2017). The MUR SST datasets have the best grid resolution, compared to most other available merged GHRSSST products.

160 Moreover, both remote sensing products have sufficient spatial grid resolution to highlight mesoscale O (20–1000 km) patterns that may arise from tidal impacts on temperature. The use of both products aims to determine which one suits the best for that purpose.

2.1.2. NEMO model: *AMAZON36* configuration

164 We used the same *AMAZON36* configuration of the NEMO ocean circulation model as in Assene et al. (2024). *AMAZON36* covers the western tropical Atlantic region with a $1/36^\circ$ (~ 3 km) horizontal grid, from the Amazon River mouth to the open ocean. The domain lies between 54.7°W – 35.3°W and 5.5°S – 10°N . The vertical grid comprises 75 vertically fixed z-coordinates levels, with finer grid refinement close to the surface, i.e., 28 levels in the first 160 m. Refer to the previous study (Assene et al., 2024) for the full description of the NEMO model and configuration keys parameters. Furthermore, note that the simulations have been extended to December 2016 to fit the long-term timescale (2007–2016) of the selected remote sensing datasets.

172 2.2. Method: harmonic analysis of temperature datasets

A signal can be understood as the superposition of variations at several frequencies from lower to higher (f_i, f_{i+1}, \dots, f_n). Harmonic analysis is a classical method used to find the variation at a given frequency (f_i) from the whole signal – the temperature data (T) in this case.

176 We used the *Sirocco Comodo Tools* (*SCT*; Allain, 2014) to perform harmonic analysis in temperature datasets and get the atlas of amplitude and phase lag associated with the two major semidiurnal (M_2 and S_2) and the dominant fortnightly (MSf) frequencies. The analysis is applied on raw data without any spatial or temporal filtering. We applied this analysis on hourly data to extract semidiurnal signals and on daily data to extract fortnightly variations.

Note that to clearly separate two waves from the original signal, a separation period defined as $t_{1,2} = |f_1 - f_2|^{-1}$ must be less than the analysis period t . Considering hourly data, the separation period between M_2 or S_2 and MSf is < 1 day, whilst it is 14.77 days between M_2 and S_2 , i.e., equal to MSf period. Then, using daily data, to properly separate MSf from its nearby other fortnightly frequency Mf (13.66^{-1} days), as well as the ~ 12 -days period aliased M_2 signal in daily data, and retrieve only the MSf signal, Ray and Susanto (2016) indicate that an analysis period of about $\frac{1}{2}$ year is needed, verified with *SCT* (~ 183 days).

188 Consequently, the duration of each dataset is sufficient to satisfy all the above conditions to analyze variability at chosen tidal frequencies.



3. Results

This section presents our findings. Note that in the following figures, the phase lag is expressed in hours rather than the conventional angular units (degrees). We converted phase lags using the following relationship: $t_{lag} = (\varphi \times T_n)/360^\circ$, where t_{lag} represents the phase lag in hours, φ denotes the phase lag in degrees, T_n is the period in hours for the respective tidal frequency n .

For the amplitudes, we adopt a significance threshold of 10^{-2} °C based on typical observation uncertainties in satellite SST products (~ 0.01 – 0.05 °C; Chin et al., 2017). Amplitudes below this threshold are classified as not significant or "noisy", whereas amplitudes above this threshold are deemed significant and categorized into three classes: weak ($>10^{-2}$ to 10^{-1} °C), strong ($>10^{-1}$ to 1 °C), and very strong (>1 °C) (Table 1).

Table 1. The significance criterion of temperature amplitude.

Amplitude (A in °C)	Significance (color shading in Fig.6)
$A \leq 10^{-2}$	<i>noisy (gray)</i>
$10^{-2} > A \leq 10^{-1}$	<i>weak (white)</i>
$10^{-1} > A \leq 1$	<i>strong (white)</i>
$A > 1$	<i>very strong (light blue)</i>

Six analysis boxes ($\sim 0.5^\circ \times 0.5^\circ$) are strategically positioned to capture the range of tidal dynamics in the NBR (see location in Fig. A1, Appendix A). These are designated as: "A-shelf" (continental shelf break at IT generation site A), "A-ocean" (offshore along IT pathway A), "B1" and "B2" (near-field and far-field locations along IT pathway B), "On-shelf" (northwestern continental shelf), and "Off-shore" (open ocean site with minimal tidal influence). Coordinates and characteristics are detailed in Table 2, and vertical temperature amplitude profiles are examined in Section 3.3.

Table 2. Coordinates and tidal characteristics of selected boxes.

Box Name	Longitude range [°W]	Latitude range [°N]	Region type	Dominant tidal process
<i>On-shelf</i>	<i>49.5–50</i>	<i>3–3.5</i>	<i>Northwestern shelf</i>	<i>Barotropic tides dissipation</i>
<i>A-shelf</i>	<i>45.75–46.25</i>	<i>0.5–1</i>	<i>shelf break (Site A)</i>	<i>IT dissipation</i>
<i>A-ocean</i>	<i>45.25–45.75</i>	<i>1.75–2.25</i>	<i>IT pathway A</i>	<i>IT propagation and dissipation</i>
<i>B1</i>	<i>41.9–42.4</i>	<i>-0.6 – -0.1</i>	<i>IT pathway B (near)</i>	<i>IT dissipation</i>
<i>B2</i>	<i>41.2–41.7</i>	<i>1.1–1.6</i>	<i>IT pathway B (far)</i>	<i>IT dissipation</i>
<i>Off-shore</i>	<i>47–47.5</i>	<i>8–8.5</i>	<i>Open ocean</i>	<i>Minimal tidal impact</i>

Each box spans $0.5^\circ \times 0.5^\circ$ (~ 3080.3 km²)



It is worth noting that all the amplitudes presented in the following was validated by comparison with spectral analysis. We used non-filtered time series taken within the six boxes presented before. The spectral analyzes were carried out with a Hamming window for SST (observations and simulations) and at 120 m depth only for the simulated temperature. We found very good agreement with harmonic analysis (not shown).

3.1. Variability at MSf frequency in remote sensing and model simulations

We firstly analyze the MSf variability which can be commonly found in long term (2007–2016) daily remote sensing and model simulations datasets. The MSf variability of SST is similar between the two observational products (MUR, Fig. 1a and TMI, Fig. 1b). The average amplitude is about 0.15 °C on the northwest of the shelf around the “On-shelf” point (48°W–52°W and 0°N–6°N) where barotropic tides induced mixing dominates, whereas, offshore regions show noisy amplitudes. The maximum values extend farther in tidal simulations, extending to “A-shore” point (Fig. 1c). For non-tidal simulations, the amplitude of MSf variability is not significant, i.e., mean value weaker than 10⁻² °C (Fig. 1d). This means that, in the NBR at the surface, the MSf variability of SST is mainly driven by barotropic tides.

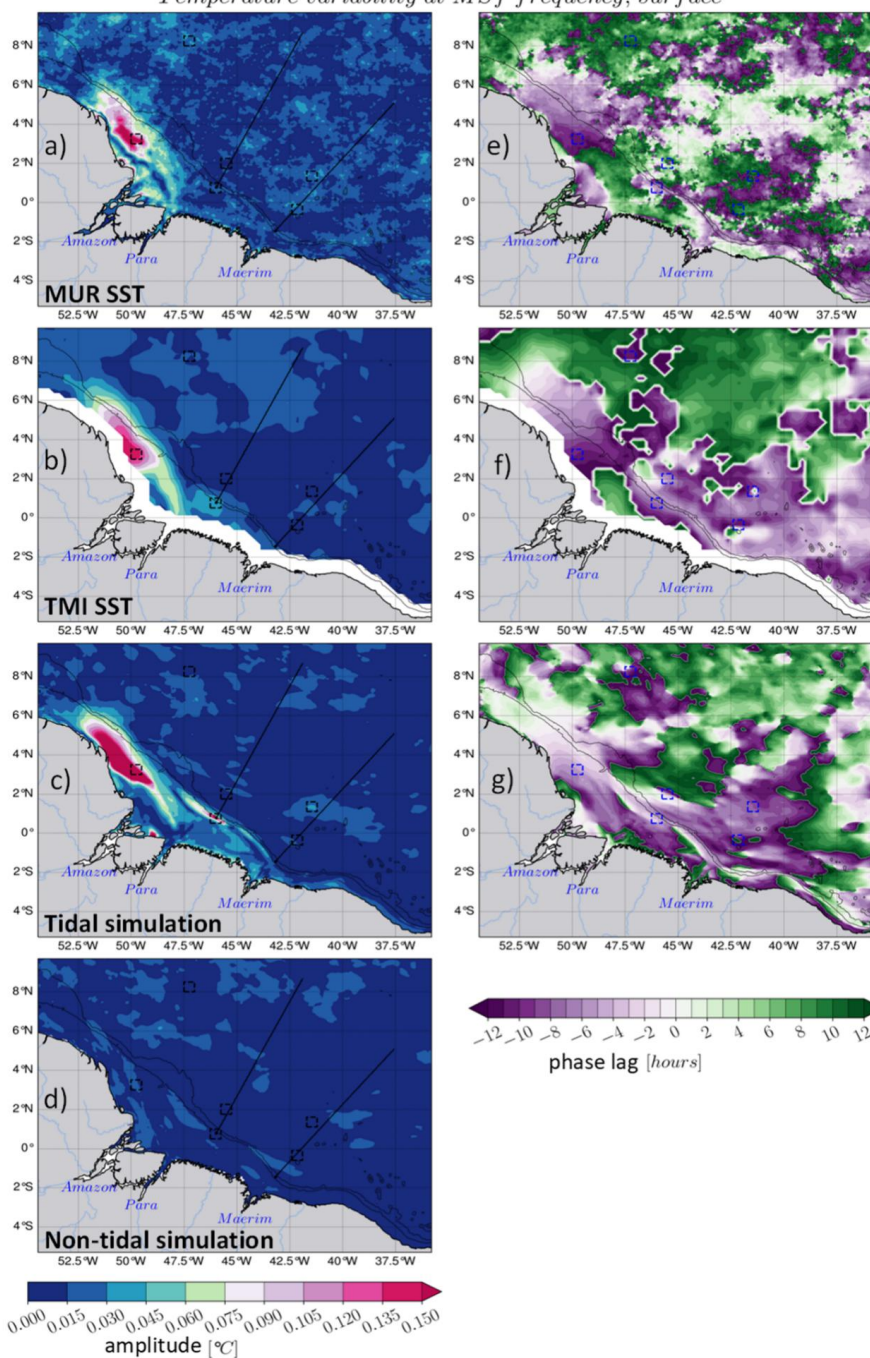
The maximum amplitude of the MSf variability for SST lags the MSf tidal currents by about -12 hours to -6 hours in the two observational products, MUR SST (Fig. 1e) and TMI SST (Fig. 1f), and the tidal simulations (Fig. 1g). This delay reflects the time for vertical mixing to redistribute heat, a process depending on mixing intensity and stratification (See Ray and Susanto, 2016). However, this phase lag has no significance for the non-tidal simulations, since the associated amplitude is also not significant.

There is an additional lag between the maximum of tidal potential and the maximum of tidal currents during Spring and Neap tides period, i.e., when they produce the maximum of mixing. This lag is called “age of the tides” and is defined as: $T_a = \frac{G_{S_2} - G_{M_2}}{1.0159}$, where G is the phase in degrees of barotropic tidal elevation for each harmonic, the denominator represents the theoretical amplitude modulation coefficient (see more details in Holloway and Merrifield, 2003 and Ray and Susanto, 2016). T_a is calculated from tidal simulations and is expressed in hours.

On the shelf, the maximum MSf amplitude values correlate with tidal ages ranging from approximately 22 hours in the north to 30 hours near the Amazon River mouth, and 22±2 hours along IT trajectories A and B (see Fig. B1 in Appendix B). As a result, the total lag between the tidal potential and the maximum of temperature variability ($t_{lag} - T_a$) ranges between ~1–1.75 days, or approximately 2 days at most.



Temperature variability at MSf frequency, surface



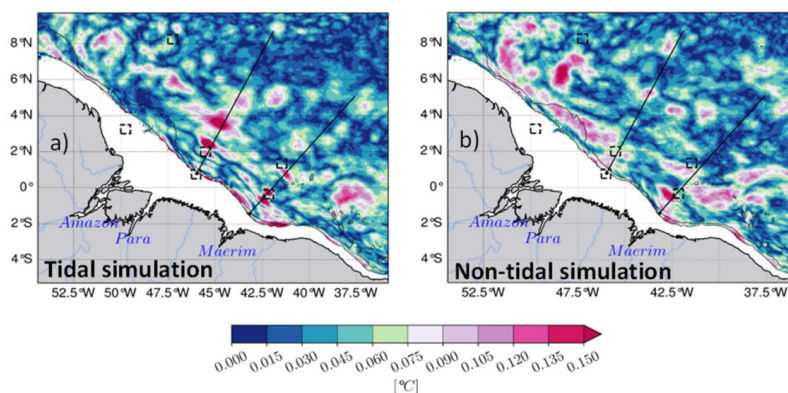


248 **Figure 1.** The harmonic analysis of sea surface temperature at fortnightly frequency (MSf, 14.77 days) based on long-term (2007–2016) daily SST. MUR SST amplitude (a) and phase lag (e), TMI SST amplitude (b) and phase lag (f), tidal simulation amplitude (c) and phase lag (g) and non-tidal simulation amplitude (d). The black dotted boxes delimit the region within the amplitude of the temperature is spatially averaged along the depth for the modeled temperature, same regions are marked in the phase lag maps. For this figure and in the following, unless otherwise stated, the two black contours represent the 200 and 2000 m isobaths from the model bathymetry

252

Looking deeper in the thermocline depth range (120 m), the two simulations with and without tidal forcing present similar amplitude, with an average value of 0.15 °C (Fig. 2). However, for the simulations with tides, the maximum values are primarily arranged in patches along IT trajectories A and B (Fig. 2a), while for the simulations without tides, maximum values follow the NBC pathway and its retroflexion (Fig. 2b), emphasizing the potential of the background circulation in shaping temperature at fortnightly frequency. This will be further discussed.

256



260

Figure 2. The amplitude of MSf variability at 120 m depth for tidal (a) and (b) non-tidal simulations.

264

Note that the harmonic analysis only gives the modulus of the amplitude, hence it is not possible to know whether cooling or warming occurs due to tidal-induced mixing. For the MSf frequency particularly, it is possible to obtain the sign of MSf variability amplitude illustrated in the figures above, thanks to a composite analysis, see details of method in Appendix C. We performed this analysis on the same daily temperature datasets. We found that the maximum MSf amplitude at the surface and in deeper layer in fact depicts a cooling, meaning that the Spring-Neap variability of barotropic tides results in temperature cooling at the surface, whereas baroclinic tides and background circulation sustain subsurface cooling in tidal and non-tidal simulations, respectively. More details on composites analysis results can be found in the Appendix C.

272



3.2. Spatial variability at S_2 and M_2 frequencies in the simulations

Using hourly model simulations, we then analyze how the temperature is spatially shaped at the semidiurnal frequencies.

276

3.2.1. Amplitude and phase lag

The atlases of temperature variability for S_2 and M_2 frequencies in tidal simulations are presented in Figure 3. For the S_2 frequency, at the surface (Fig. 3a), the maximum amplitude (~ 0.12 °C) is observed over the north-western shelf, near the “On-shelf” location (between 2.5° – 5° N), while lower amplitudes ($< 6 \times 10^{-2}$ °C) prevail elsewhere. The associated phase lag (Fig. 3b) indicates a mean lag of approximately 6 hours, meaning the maximum occurs during or after high and low tides. Deeper near the thermocline (~ 120 m), stronger amplitude with mean value of about 0.6 °C is observed (Fig. 3c). They are horizontally collocated with the patches of IT dissipation and the maximums of baroclinic sea surface height (SSH) at the S_2 frequency (Fig. S1c, Supplementary 1). The associated phase lag (Fig. 3d) indicates a lag of ± 6 hours for these amplitude maximums, and moreover it resembles the phase lag of the S_2 baroclinic SSH (see details in Appendix B, Fig. B1).

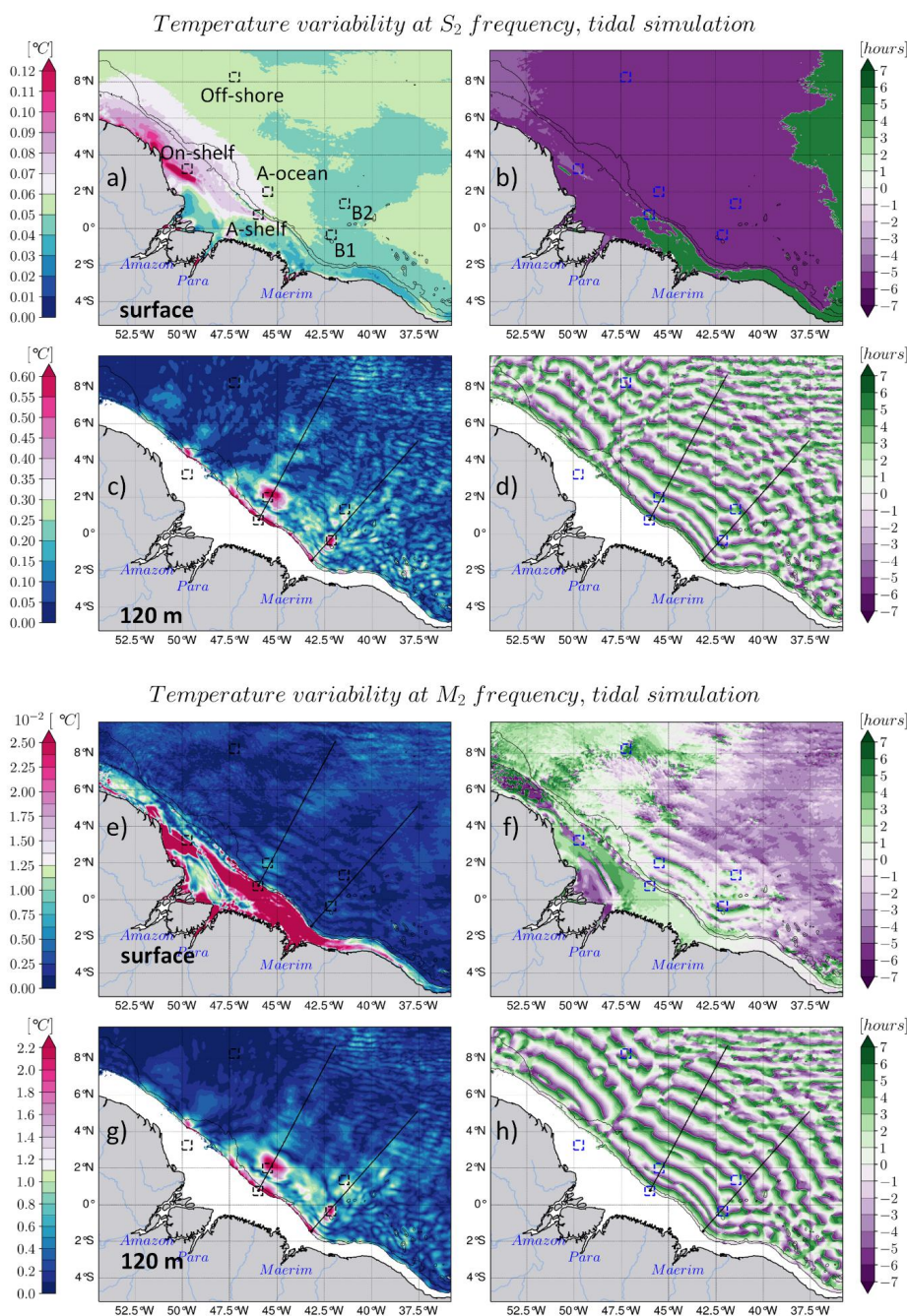
For the M_2 frequency, at the surface, we observe lower but significant maximums ($\sim 2.5 \times 10^{-2}$ °C) over the entire shallow shelf (Fig. 3e) where barotropic tides dissipate (Fig. A1a in Appendix A) and create mixing. Offshore, some lower amplitudes ($> 10^{-2}$ °C) are observed along IT trajectory A (Fig. 3e). The associated phase lag shows a lag of ± 3 hours (Fig. 3f), indicating that these maximums occur during the mid-tide, i.e., when the tidal potential is at its maximum.

As seen for S_2 , the amplitude at the M_2 frequency is higher near the thermocline compared to the surface, but with values three orders of magnitude stronger (~ 2.2 °C, Fig. 3g). Similarly, these M_2 variability maximums are collocated with dissipation patches of ITs and the maximums of baroclinic SSH for M_2 tides. We also found a phase lag close to that of the S_2 variability at the same depth for M_2 variability (Fig. 3h).

296 These findings clearly indicate that the ITs are responsible for the strong and very strong subsurface amplitudes observed at respective frequency.

Note that the simulations without tides exhibit similar amplitude at the surface for S_2 frequency as in tidal simulations, with mean values of approximately 0.12 °C located from the mouth of the Amazon to the northwestern shelf (Fig. S2a, Supplementary 2). Lower values (< 0.06 °C) are observed elsewhere in the region, and noisy signal ($< 10^{-2}$ °C) deeper (Fig. S2c, Supplementary 2). For the M_2 frequency, the amplitudes are noisy at the surface as well as at the subsurface (Fig. S2b and d, Supplementary 2).

300



304

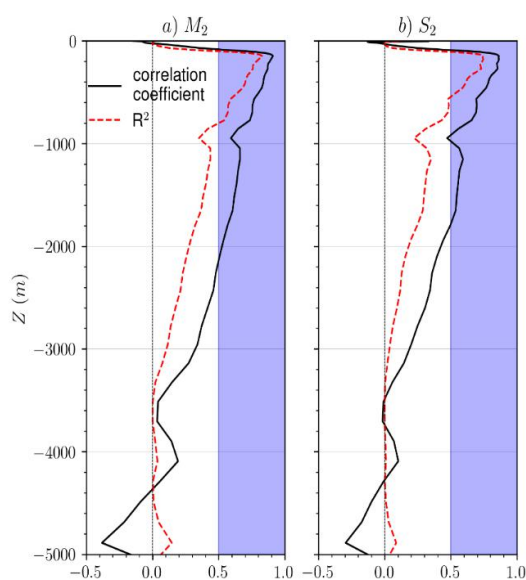
Figure 3. The harmonic analysis of temperature at S_2 frequency based on 2015 tidal simulation hourly datasets: amplitude (a) and phase lag (b) at surface, amplitude (c) and phase (d) at 120 m depth, same for M_2 frequency in



308 lower panels (e, f, g, and h, respectively). The black and blue boxes delimit the $0.5^\circ \times 0.5^\circ$ area, as defined in
Table 2, within the amplitude of the temperature is averaged along the depth. Hereinafter in the figures above,
unless otherwise stated, the black thin contours are the 200 and 2000 m isobaths, while the two straight lines
represent the two main pathways of internal tides.

312

Since we noted a spatial collocation between IT's SSH amplitude and temperature variability amplitude, we
therefore compute the correlation between them over the full domain and along the depth, see Figure 4. This
correlation highlights the close link between ITs and temperature variability for the high frequencies, M_2 (Fig.
316 4a) and S_2 (Fig. 4b). Between the subsurface (> 60 m) and up to ~ 800 m depth for M_2 and up to ~ 600 m for S_2 ,
there is a very strong positive and significant correlation, reaching its maximum in the thermocline layer (100–
180 m) (Fig. 4). The correlation coefficient and its significance level are 0.91 and 0.86 for M_2 and, 0.83 and 0.75
for S_2 , respectively (Fig. 4). This implies that the horizontal structure of temperature variability in subsurface
320 layers closely follows that of the baroclinic SSH at the surface. This is a further proof of ITs as dominant driver
shaping temperature off the Amazon shelf break.



324

Figure 4. Correlation between the amplitude of IT baroclinic SSH at the surface and the amplitude of the
temperature variability for the whole domain and throughout the depth for semi-diurnal frequencies M_2 (a) and
 S_2 (b). The black solid line represents the correlation and red dashed line represents its significance; the blue
328 color shading indicates significant values (≥ 0.5) for both.

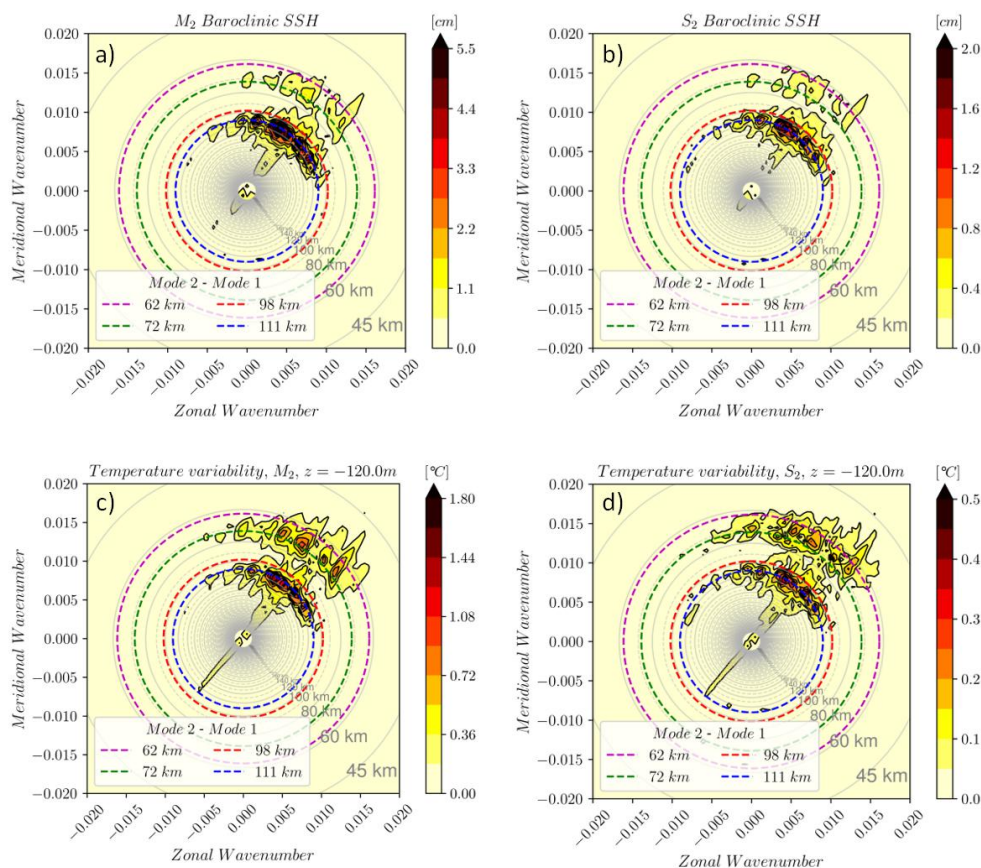


3.2.2. Wavelengths in high-frequency variability

To further characterize the impact of ITs on temperature, we analyzed the horizontal wavelength involved in IT surface elevation and compare it to what exists in temperature variability for the two semi-diurnal frequencies. We used a 2D fast Fourier transform in complex fields (from amplitude and phase lag) of temperature variability and baroclinic SSH to extract the wavelengths and the direction of propagation.

Figure 5a shows dominant northeastward propagation for the M_2 baroclinic elevation between 110–120 km and 60–80 km wavelengths, corresponding to IT of mode-1 and mode-2 wavelengths, respectively, in good agreement with Barbot et al. (2021). The direction of propagation and the dominant wavelengths are roughly the same for S_2 IT SSH imprints, nevertheless with wider range of wavelengths for mode-1 (100–120 km, Fig. 5b).

At 120 m depth, temperature variability presents 100–120 km and 60–80 km wavelengths for M_2 (Fig. 5c), and between 100–120 km and 50–80 km wavelengths for S_2 (Fig. 5d). As with SSH, these ranges correspond to mode-1 and mode-2 northeastward propagation. However, mode-2 signals are more pronounced in temperature than in SSH. These findings constitute additional evidence of the impact of tides especially internal tides in temperature high-frequency variability.



344



Figure 5. Two-dimensional normalized power spectral density of the baroclinic SSH (upper panels) and temperature variability at 120 m (lower panels) for M_2 (left panels) and S_2 (right panels) semi-diurnal frequencies. The gray rings represent the horizontal wavelength grid scale, and the colored rings represent the horizontal wavelengths of modes 1 and 2. The color shading stands for the amplitude.

3.3. Mean along-depth profile of temperature amplitudes

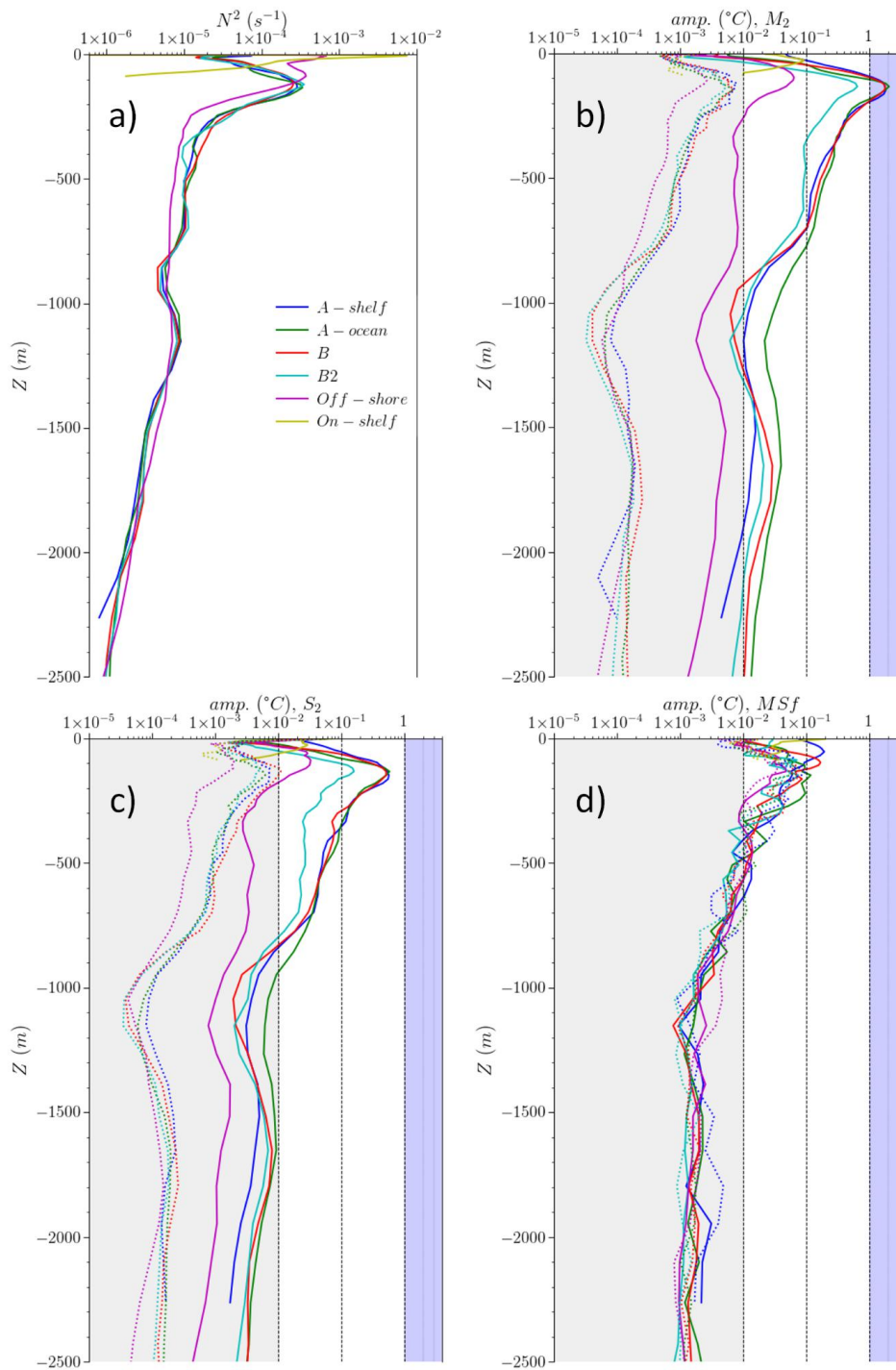
To characterize the temperature variability amplitude from the surface to deeper layers, we finally describe the mean along-depth profile of amplitude for the three frequencies, using only model simulations. The average is performed within the six contrasted boxes, regarding their tidal characteristics (see Table 2), and along the depth for the amplitude of the temperature variability as well as the squared Brunt-Väisälä frequency $N^2 = \left(-\frac{g}{\rho} \partial_z \rho\right)$, where g is the acceleration due to gravity and ρ is the density. Note that looking at N^2 serve to emphasizes the link between subsurface maximum amplitudes and the pycnocline depth range. Note that N^2 is calculated only for the simulations including tides.

N^2 peaks in the subsurface within the thermocline depth range (100–200 m; Magalhaes et al., 2016 and Tchilibou et al., 2022) with an average value ranging between $\sim 2\text{--}3 \times 10^{-4} \text{ s}^{-1}$ for all boxes except for "On-shelf" and "Off-shore". For the two latter shallower locations the peak occurs near the surface with mean values of $\sim 7 \times 10^{-4} \text{ s}^{-1}$ and $> 10^{-2} \text{ s}^{-1}$, respectively, (Fig. 6a). Note that a similar vertical structure is observed for N^2 in the simulations without tidal forcing (not shown).

This vertical profile is reproduced by temperature amplitude in both simulations and for the three frequencies, M_2 (Fig. 6b), S_2 (Fig. 6c), and MSf (Fig. 6d). For the simulations without tides (dotted lines in panel b to d), the amplitudes are not significant ($\leq 10^{-2} \text{ }^\circ\text{C}$) for all the boxes and for the two semidiurnal frequencies, while for MSf frequency it reaches mean amplitude of $\sim 0.1 \text{ }^\circ\text{C}$ within the thermocline depth range, comparable to that of the tidal simulations (Fig. 6d).

Regarding the semidiurnal frequencies, for the simulations including tides, the mean amplitude is mainly strong within the thermocline depth range reaching $\sim 0.5 \text{ }^\circ\text{C}$ for S_2 and $\sim 2 \text{ }^\circ\text{C}$ for M_2 . The maximum amplitude obtained with model in the thermocline depth range (100–200 m, including pycnocline) align well with the maximum IT shear instability and resulting peak of the energy dissipation within the pycnocline as recently observed at same location by Kouogang et al. (2025).

Furthermore, there is a notably difference in the vertical extent of significant amplitudes ($> 10^{-2} \text{ }^\circ\text{C}$) across frequencies. The vertical extent involved in temperature variability is about 2.5 km for M_2 , approximately the half for S_2 (0.8–1 km) and less for MSf (0.6–0.8 km). This likely depicts the average vertical length scale potentially affected by tidal mixing caused by the energy loss of ITs.





380 **Figure 6.** The vertical profiles (a) the squared Brunt-Väisälä frequency and the amplitude of temperature
variability at (b) M_2 , (c) S_2 and (d) MSf frequencies averaged inside the boxes defined in Table 2 and illustrated
in Fig. A1a in Appendix A. The tidal and non-tidal simulations are represented by solid and dotted lines,
respectively. In panels (a), (b) and (c), gray color shading stands for not significant values ($\text{amp.} \leq 10^{-2} \text{ } ^\circ\text{C}$), white
color shading is for weak ($10^{-2} \text{ } ^\circ\text{C} < \text{amp.} \leq 0.1 \text{ } ^\circ\text{C}$) and strong values ($0.1 \text{ } ^\circ\text{C} \text{ amp.} \leq 1 \text{ } ^\circ\text{C}$), and light blue stands
384 for very strong values ($\text{amp.} > 1 \text{ } ^\circ\text{C}$) as in Table 2.

388 **4. Discussion and Conclusion**

This study provides the first comprehensive regional characterization of temperature variability at tidal
frequencies (M_2 , S_2 , and MSf) across the northern Brazilian region, based on satellite sea surface temperature
(SST) observations and twin numerical simulations with and without tidal forcing. This combined framework
392 enables direct attribution of temperature variability to barotropic tides, internal tides (ITs), and sometimes
background circulation, revealing distinct surface and subsurface responses across the shelf–open ocean system.
These results further demonstrate how high-frequency tidal processes exert a major influence on upper-ocean ($<$
1000 m) temperature variability across the northern Brazilian region (NBR). Further important implications can
396 be drawn for heat redistribution, biogeochemical feed-backs, and the interpretation of satellite observations in
strongly tidal tropical environments.

4.1. On the fortnightly temperature variability

Fortnightly MSf variability displays consistent surface amplitudes of about $0.15 \text{ } ^\circ\text{C}$ over the northwestern shelf
400 in both satellite products (MUR, TMI) and in simulations including tidal forcing. These values align with ranges
reported in other strongly tidal environments, from $0.1\text{--}0.5 \text{ } ^\circ\text{C}$ in the Indonesian Seas (Ray and Susanto, 2016;
Nugroho et al., 2018; Susanto and Ray, 2022) to $0.1\text{--}0.3 \text{ } ^\circ\text{C}$ in the South China Sea (Susanto et al., 2019). In the
NBR, MSf temperature fluctuations likely arise from the Spring–Neap modulation of barotropic tidal current
404 shear over the shelf, mechanisms previously described for confined straits and shallow shelves (Holloway and
Merrifield, 2003; Ruault et al., 2020). Unlike most case studies, this region extends this phenomenology to a
transition zone where barotropic processes dominate the inner shelf while ITs exert increasing control offshore.
In the other hand, at the surface layers, amplitudes are not significant along IT pathways, this may reflect a
408 rapid atmospheric heat flux adjustment that counteracts internal tide–induced cooling and/or the inherently
incoherent character of IT dynamics that disperses energy across frequencies, preventing harmonic methods, that
point to a unique frequency, from capturing a clear MSf signature.

At depth, tidal simulations detect MSf amplitudes of similar magnitude ($\sim 0.15 \text{ } ^\circ\text{C}$) along IT pathways. These
412 subsurface signatures reflect the Spring–Neap modulation of baroclinic tidal energy flux, which varies by about
50 percent between Spring (16 kW.m^{-1}) and Neap (8 kW.m^{-1}) periods (Tchilibou et al., 2022). Such subsurface
MSf temperature variability associated with ITs has not been documented previously.

Surprisingly, non-tidal simulations exhibit fortnightly signals of similar amplitude along the North Brazil
416 Current pathway, suggesting circulation-driven variability, possibly through advection, as indicated at seasonal



time scales (Assene et al., 2024), or through mean baroclinic shear (Kouogang et al., 2025). In simulations including tides, this circulation-driven signature is reduced or redistributed across frequencies, implying an interaction between background flow and tidal processes (Kouogang et al., 2025b). MSf variability extends to
420 depths of roughly 600-800m depth—shallower than semidiurnal signals—but its maximum expression occurs within the thermocline (100–200 m), suggesting potential implications for euphotic zone processes.

In summary, fortnightly temperature variability in the NBR arises from barotropic processes over the shelf and from ITs offshore, with subsurface MSf variability along IT pathways documented for the first time.

424 Composite analyzes give the sign of MSf variability and indicate a net cooling of similar magnitude, though subsurface amplitudes retrieved from composites slightly exceed those from harmonic analysis. This difference could reflect the influence of background circulation, which is better expressed in daily composite frameworks than in frequency-isolating harmonic methods or/and the impact of incoherent IT-induced mixing. Nevertheless,
428 the two approaches reveal a consistent 2–3 day lag between tidal forcing and maximum thermal response. Identical delays have been reported elsewhere for suspended sediment (Shi et al., 2011), nutrient injections and chlorophyll responses (Sharples et al., 2007).

Furthermore, it is worth noting that as most MSf studies average over narrow windows centered on Spring/Neap
432 dates (e.g., Souza and Pineda, 2001; Ruault et al., 2020), the strongest impacts may be underestimated. We therefore recommend future Spring–Neap studies to apply a lag-resolved approaches spanning ± 3 days, meaning $\{-3, -2, -1, 0, 1, 2, 3\}$, recognizing that optimal lags may vary with regional tidal age and mixing response timescales (see Appendix C).

436 **4.2. On the semidiurnal temperature variability**

At semidiurnal frequencies, contrasting regimes emerge across the shelf and the open ocean. Over the shallow northwestern shelf, barotropic tidal mixing produces very weak M_2 surface amplitudes ($\sim 2.5 \times 10^{-2}$ °C) and moderate S_2 amplitudes (~ 0.12 °C). These values are markedly smaller than those reported for classic shelf seas,
440 such as the Irish Sea (Simpson and Bowers, 1981) or Yellow Sea (Li et al., 2020), and likely reflect intense air–sea heat exchange in such convergence zone (Koch-Larrouy et al., 2007; Sprintall et al., 2014, 2019) therefore reducing the high-frequency surface temperature amplitude.

In other hand, the persistence of detectable S_2 signals in both tidal and non-tidal simulations suggests a
444 contribution from radiational tides (Arbic, 2005; Balidakis et al., 2022).

Offshore, ITs dominate semidiurnal variability. Subsurface amplitudes reach approximately 2.2 °C for M_2 and 0.6 °C for S_2 at thermocline depth, values exceeding most in situ estimates reported elsewhere for similar depths (van Haren et al., 2016; Purwandana et al., 2021; Smith et al., 2016). These subsurface hot-spots spatially
448 coincide with generation and dissipation zones and the elevated dissipation rates ($\epsilon \sim 10^{-7}$ W.kg $^{-1}$; Kouogang et al., 2025) documented during the AMAZOMIX cruise—values 10–100 times above background levels.

4.3. On the along-depth profile of temperature variability

The depth extent of significant temperature variability decreases systematically with tidal period, consistent with
452 energy distribution: M_2 , which represents about 70 percent of total tidal energy (Beardsley et al., 1995; Gabioux



et al., 2005; Fassoni-Andrade et al., 2023), penetrates to around 2.5 km, whereas S_2 reaches about 1 km and MSf around 0.6–0.8 km. These contrasts indicate that the capacity of tidal motions to influence the water column depends strongly on the available energy at each frequency and points to a frequency-dependent control of deep-ocean mixing and heat redistribution. Elevated dissipation could remain mostly confined above ~670 m, suggesting that mixing within the thermocline drives the largest impacts while deeper signals likely involve vertical advection by the background circulation, consistent with seasonal-scale findings (Assene et al., 2024). These characteristics align the NBR with known deep-ocean IT-influenced areas such as the Hawaiian Ridge (Holloway and Merrifield, 2003), Luzon Strait (Alford et al., 2015), and the Andaman Sea (Jithin and Francis, 2020).

Correlations between SSH and subsurface temperature amplitudes > 0.5 persist to depths of ~2000 m for M_2 and ~1800 m for S_2 , with maximum values within the thermocline, confirming the central role of ITs in structuring semidiurnal offshore temperature variability.

4.4. On the wavelength in temperature variability

Two-dimensional fast Fourier transform analyzes indicate that subsurface temperature variability reproduces both mode-1 and mode-2 IT wavelengths and propagation directions, consistent with SSH signatures (Barbot et al., 2021). Mode-2 signals (50–80 km) appear more expressive in subsurface temperature than in SSH, suggesting that modeled temperature fields may serve as an alternative pathway for detecting higher baroclinic modes, though confirmation from moorings, gliders, or Argo deployments will be required.

472 5. Perspectives

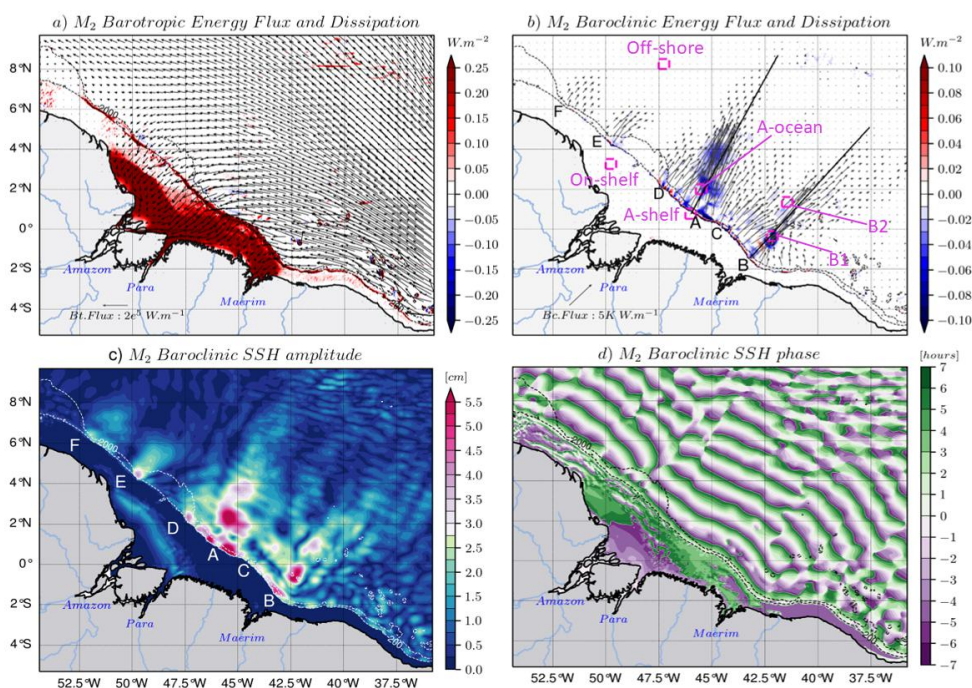
From a methodological perspective, despite a 25-fold difference in spatial resolution (~1 km MUR vs. ~25 km TMI), both satellite SST products yield consistent MSf amplitude patterns. TMI's longer record benefits retrospective analysis, while MUR's finer spatial resolution is advantageous for resolving higher baroclinic modes. The numerical configuration captures the main barotropic and baroclinic tidal features and seasonal temperature patterns of the region (Assene et al., 2024), and the location of modeled dissipation hot-spots aligns with recent AMAZOMIX observations (Kouogang et al., 2025). However, harmonic analysis extracts only the coherent, phase-locked ITs (Zaron, 2017; Buijsman et al., 2017). Incoherent ITs generated by interaction with eddies or strong current-topography interactions (Zaron, 2017; Buijsman et al., 2017 and Kouogang et al., 2025b) likely enhance semidiurnal temperature variability beyond the levels estimated here. Direct comparisons with mooring records from dissipation hot-spots will clarify this component.



Appendices

484

Appendix A. Characteristics of M_2 coherent tides in the northern Brazilian region (NBR)



488

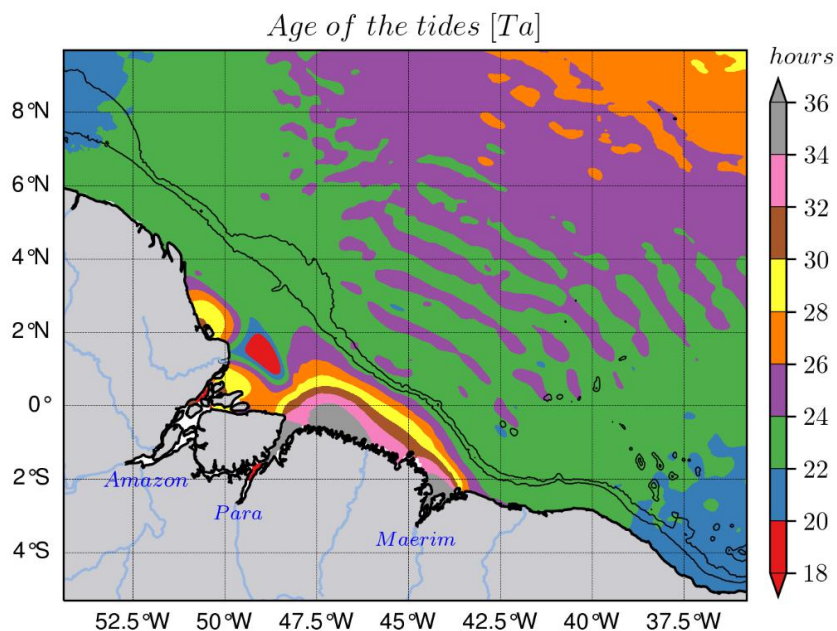
Figure A1. Characteristics of M_2 coherent tides for the year 2015: (a) barotropic energy flux (black arrows) and barotropic energy dissipation (color shading), (b) depth-integrated baroclinic energy flux (black arrows) and depth-integrated baroclinic energy dissipation (color shading), (c) baroclinic sea surface height and (d) its phase lag. A to F labels in panels (b) and (c) indicate the internal tide generation sites on the shelf break. Black and white dotted lines in respective panels represent the 200 and 2000 m isobaths from the model bathymetry. In panel (b) and for figures above, the two black straight lines indicate the mean trajectory of internal tides radiating from generation sites A and B; magenta (here) and black (in the following figures) boxes indicate the areas within the vertical mean of temperature amplitudes were performed (see Section 3.3); the center of each box corresponds to the location of the point for which we performed spectral analysis.

492

496



Appendix B. The age of the tides in NBR



500

Figure B1. The age of the tides (T_a) computed based on the M_2 and S_2 barotropic elevation phase from tidal simulations. T_a is about $24\text{h} \pm 2\text{h}$ (~ 1 day) in the internal tide generation sites, along their pathways and from 22h–30h over the north-western domain. Which means that in NBR, the maximum of MSf tidal currents lag the astronomical potential by about 1–1.25 days. Tin black lines are the 200 and 2000 m isobaths from model bathymetry.

504



Appendix C. Spring-Neap composites of temperature

508 • **Method of calculation**

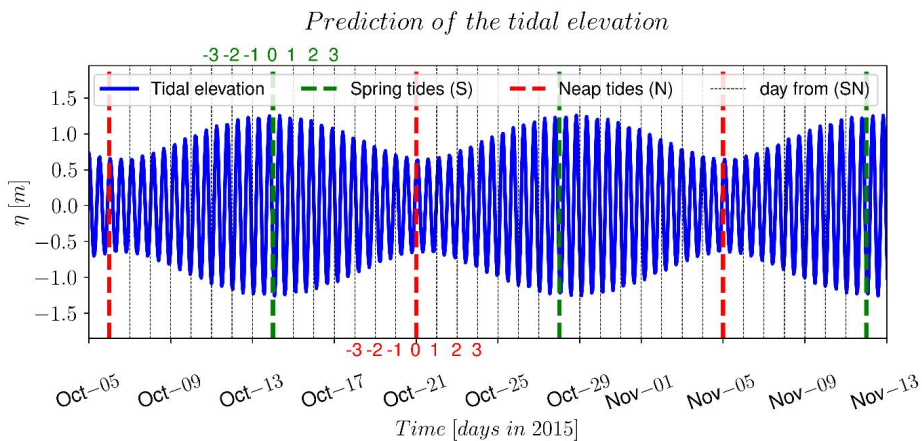
Another way to analyze the effect of the fortnightly modulation of the tidal currents on temperature daily datasets is by performing temperature Spring-Neap composite analysis. This is calculated as follows:

$$T_{Si}, T_{Ni} = \sum T_{Si}, \sum T_{Ni} \quad (D1)$$

$$\Delta T_i = \overline{T_{Si}} - \overline{T_{Ni}} \quad (D2)$$

Where $i = \{-3, -2, -1, 0, 1, 2, 3\}$, $i \in \mathbb{Z}$, is the offset in days from the Spring (S) or Neap (N) time (see illustration in Fig. C1), T is the daily temperature, the upper bar indicates the average temperature in the time series for each case of i with respect to the Spring and Neap time. We calculated the composites (ΔT) for each case of i from the long-term temperature. Compared to harmonic analysis, this method has the advantage of providing the sign of the Spring-Neap variability of the temperature, and can therefore highlights whether cooling or warming occurs.

520



524 **Figure C1.** Prediction of the barotropic tidal elevation at the NBR shelf [45.5°W, 1°N], using SCT, showing the
 Spring-Neap modulation (~14–15 days) of the elevation amplitude. The green and red solid lines indicate Spring
 and Neap tides time, respectively. The black dotted lines correspond to the days between consecutive Spring and
 Neap tides. The numbers in green and red indicate the corresponding lag from the time of Spring and Neap tides
 528 respectively.

532

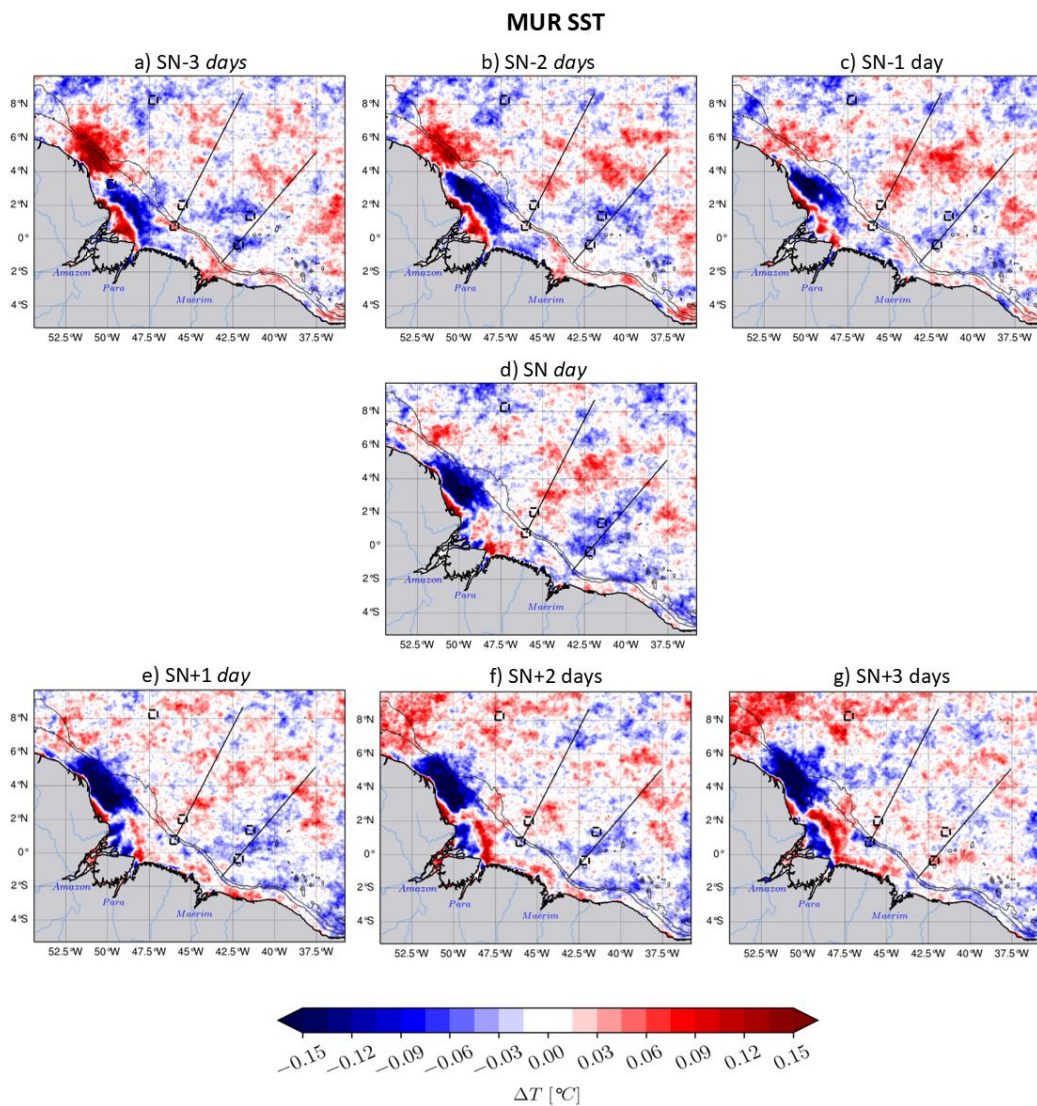


- **Amplitude and sign of temperature's Spring-Neap variability**

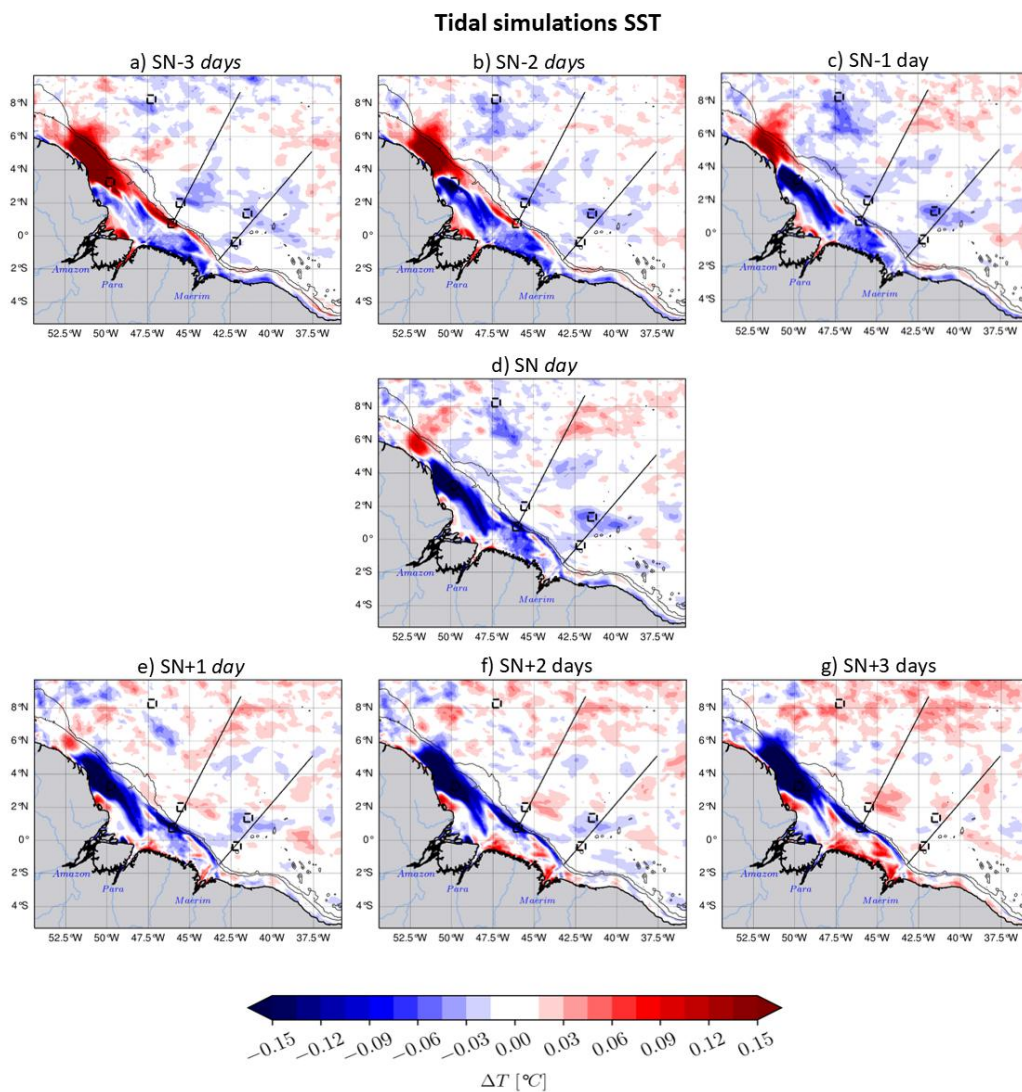
The Figures C2 and C3 presents the Spring-Neap composites computed from daily MUR SST and tidal simulations SST, respectively, for different cases of the daily offset i . Overall, for the observations and tidal simulations, the position of the maximums and their average intensity (± 0.15 °C) in the composites are similar to MSf amplitude from harmonic analysis (see Fig. 1). In non-tidal simulations SST, the intensity is very low throughout the domain ($< \pm 0.03$ °C, Fig. S3-2, Supplementary 3), in good agreement with the harmonic analysis (Fig. 1d).

Additionally, there is a variation in intensity on the composites depending on the offset from the Spring-Neap time. On the third day before the Spring-Neap (SN-3), there is a dipole (± 0.15 °C) northwest of the plateau, more visible in tidal simulations (Fig. C3) and TMI SST (Fig. S3-1, Supplementary 3) compared to MUR SST (Fig. C2), which gives way to a cooling of about 0.15 °C. This cooling extends as we approach the day of the Spring-Neap (SN) and reaches its maximum in the following days. The most significant Spring-Neap variability in composites is observed between the second (SN+2) and third day (SN+3) after the Spring-Neap (Fig. C2f-g, Fig. C3f-g and Fig. S3-1f-g, Supplementary 3). It is more evident that the maximum is reached on the third day after the Spring-Neap, given the higher intensity over the continental shelf and along the Amazon plume (Fig. C2f-g, Fig. C3f-g and Fig. S3-1f-g, Supplementary 3).

In the subsurface (~ 120 m depth), for the simulations with tides, the intensity in the Spring-Neap composites follows the same variation as at the surface based on the offset i (Fig. S3-3, Supplementary 3). The mean values (0.15 °C) are located along IT pathways A and B, with sparse maximums (up to ~ 0.3 °C) in the same locations (no shown). These differences could result from (i) the additional effect of background circulation which is more significant at this depth (see Section. 3.1 and Fig. 2). This is illustrated by the composites of non-tidal simulation temperatures showing meso- and submesoscale patterns throughout the domain (Fig. S3-4, Supplementary 3). The second explanation could be (ii) the incoherent IT impact on temperature, which is not captured by the harmonic analysis, but seems to be revealed by composite analyzes.



560 **Figure C2.** Spring-Neap composites of observed MUR SST. Each panel corresponds to a case of i , $\{-3, -2, -1, 0, 1, 2, 3\}$ respectively the offset from Spring and Neap tides time (SN), as illustrated in Fig. C1.



564 **Figure C3.** Same as Figure C2, but for tidal simulation's SST.

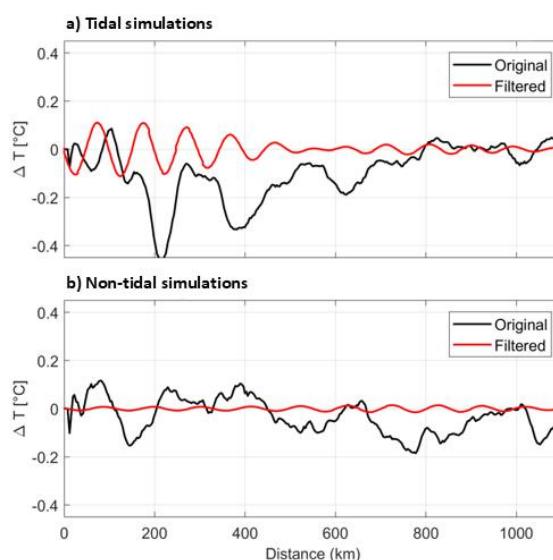
568

In the subsurface, ITs are further delineated in composite analyzes through the application of one-dimensional horizontal band-pass filtering along IT propagation pathways. This filtering procedure was implemented to isolate wavelengths of 100–120 km, characteristic of mode-1 IT signatures. In tidal simulations (Fig. C4a), pronounced oscillations with substantial amplitudes ($> 0.2^{\circ}\text{C}$) are observed within the initial 300–400 km of propagation, followed by systematic attenuation at greater offshore distances. These results are consistent with

572



576 the findings of Tchilibou et al. (2022), who demonstrated that approximately 50% of IT energy dissipation occurs within the first 300 km from the continental slope along propagation pathway A. As expected, simulations without tides (Fig. C4b) exhibit very weak oscillations, likely attributable to mesoscale variability of temperature. It should be noted that comparable results are obtained for alternative offset configurations i (not shown).



580

Figure C4. 1D horizontal of Spring-Neap composites ($i = +3$) along IT trajectory A (see black bold line in Fig. 1b) at 120 m depth for (a) tidal and (b) non-tidal simulations. The original signal is filtered using a band-pass filtering, selecting wavelengths from 100 to 120 km.

584

- **Important note**

588 The maximum cooling or warming effect on temperature resulting from Spring-Neap variability of tidal currents does not happen on the actual Spring-Neap days but rather typically occurs 2-3 days afterward. Our findings indicate that the Spring-Neap composites analysis of ocean tracers that focus exclusively on the Spring-Neap days, or averaging over one or two days surrounding (e.g.: Sharples et al., 2007 and Ruault et al., 2020)
592 inadequately capture the full amplitude of this variability. To achieve a more comprehensible understanding of Spring-Neap variability, investigations must consider individually the days surrounding the Spring and the Neap tides, i.e., follow the present methodology.



596 **Data availability statements.** All the remote sensing sea surface temperature products are publicly available
online. TMI SST v7.1 data are available from <https://www.remss.com/missions/tmi/>, was accessed on 27 June
2022. MUR SST data can be downloaded through the NASA-PODAAC platform
600 <https://podaac.jpl.nasa.gov/dataset/MUR-JPL-L4-GLOB-v4.1>, was accessed 3 December 2020. The numerical
simulations are available upon request by contacting the corresponding author.

Code availability. *Sirocco Comodo Tools (SCT; Allain, 2014)* are available online from [https://sirocco.obs-
mip.fr/other-tools/prepost-processing/comodo-tools/](https://sirocco.obs-mip.fr/other-tools/prepost-processing/comodo-tools/), last access in January 2021.

604 **Authors contributions.** Funding acquisition: AKL; Conceptualization and methodology: FA, AKL, ID and
MT; Numerical simulations: GM and FA, with assistance from JC and AKL; Formal analysis: FA with
contributions from AKL, ID, MT, SB, CRdM, EZ and interactions from all co-authors; Preparation of the
manuscript: FA with contributions from all co-authors.

608 **Conflicts of Interest.** The authors declare no conflict of interest. The founders had no role in the design of the
study; in the collection, analyzes, or interpretation of data; in the writing of the manuscript, or in the decision to
publish the results.

612 **Acknowledgments.** The Authors would like to thank the Remote Sensing System (REMSS) for providing TMI
SST datasets, and NASA's Jet Propulsion Laboratory (JPL) for providing MUR SST data. Finally, we would
like to thank the European Consortium of five institutes from France (Mercator Ocean International and CNRS),
616 Italy (CMCC) and UK (MetOffice and NOC) for the maintaining and continuous development of the NEMO
ocean general circulation model.

Funding. This work is part of the now defended PhD Thesis of FA, was co-founded by the French Institute of
620 Research for Development (IRD) and Mercator Ocean International (MOi), under the co-advising of AKL and
ID. The numerical simulations were founded by CNES/CNRS/IRD via the projects A008011357 and
A013011357 and were performed thank to "Jean-Zay", the CNRS/GENCI/IDRIS platform for modeling and
computing.



624 References

- Allain, D.J.: T-UGOm TidalToolbox, [Software] (Tech. Rep.), retrieved from <https://www5.obs-mip.fr/wp-content-omp/uploads/sites/12/2016/10/ttb-1.pdf>, 2014.
- 628 Arbic, B. K.: Atmospheric forcing of the oceanic semidiurnal tide, *Geophysical Research Letters*, 32(2), <https://doi.org/10.1029/2004GL021668>, 2005.
- Assene, F., Koch-Larrouy, A., Dadou, I., Tchilibou, M., Morvan, G., Chanut, J., Costa da Silva, A., Vantrepotte, V., Allain, D., and Tran, T.-K.: Internal tides off the Amazon shelf – Part 1: The importance of the structuring of ocean temperature during two contrasted seasons, *Ocean Sci.*, 20, 43–67, <https://doi.org/10.5194/os-20-43-2024>, 2024.
- 632 Baines, P.G.: On internal tide generation models. *Deep Sea Research Part A, Oceanographic Research Papers*, 29, 307–338, [https://doi.org/10.1016/0198-0149\(82\)90098-X](https://doi.org/10.1016/0198-0149(82)90098-X), 1982.
- 636 Balidakis, K., Sulzbach, R., Shihora, L., Dahle, C., Dill, R., Dobslaw, H.: Atmospheric contributions to global ocean tides for satellite gravimetry, *Journal of Advances in Modeling Earth Systems*, 14(11), <https://doi.org/10.1029/2022MS003193>, 2022.
- Balidakis, K., Sulzbach, R., Dobslaw, H., Dill, R.: How Do Atmospheric Tidal Loading Displacements Vary Temporally as well as Across Different Weather Models?, In: Freymueller, J.T., Sánchez, L. (eds) *Gravity, Positioning and Reference Frame, REFAG 2022*, International Association of Geodesy Symposia, vol 156, Springer, Cham., https://doi.org/10.1007/1345_2023_201, 2023.
- 640 Barbot, S., Lyard, F., Tchilibou, M., Carrere, L.: Background stratification impacts on internal tide generation and abyssal propagation in the western equatorial Atlantic and the Bay of Biscay, *Ocean Science*, 17, 1563–1583, <https://doi.org/10.5194/os-17-1563-2021>, 2021.
- 644 Beardley, R.C., Candela, J., Limeburner, R., Geyer, W.R., Lentz, S.J., Castro, B.M., Cacchione, D., Carneiro, N.: The M2 tide on the Amazon Shelf, *Journal of Geophysical Research: Oceans*, 100, 2283–2319, <https://doi.org/10.1029/94JC01688>, 1995.
- 648 Buijsman, M.C., Arbic, B.K., Richman, J.G., Shriver, J.F., Wallcraft, A.J., Zamudio, L.: Semidiurnal internal tide incoherence in the equatorial Pacific, *Journal of Geophysical Research: Oceans*, 122, 5286–5305, <https://doi.org/10.1002/2016JC012590>, 2017.
- 652 Cazenave, F., Zhang, Y., McPhee-Shaw, E., Bellingham, J.G., Stanton, T.P.: High-resolution surveys of internal tidal waves in Monterey Bay, California, using an autonomous underwater vehicle, *Limnology and Oceanography: Methods*, 9, 571–581, <https://doi.org/10.4319/lom.2011.9.571>, 2011.
- Chelton, D.B., Wentz, F.J.: Global Microwave Satellite Observations of Sea Surface Temperature for Numerical Weather Prediction and Climate Research, *Bulletin of the American Meteorological Society*, 86, 1097–1116, <https://doi.org/10.1175/BAMS-86-8-1097>, 2005.
- 656 Chin, T.M., Vazquez-Cuervo, J., Armstrong, E.M.: A multi-scale high-resolution analysis of global sea surface temperature, *Remote Sensing of Environment*, 200, 154–169, <https://doi.org/10.1016/j.rse.2017.07.029>, 2017.
- 660 Doodson, A.T., Warburg, H.O.: Admiralty Manual of Tides, H. M. Stationery Office, London, 270, 1941.
- Duda, T.F., Lin, Y.-T., Buijsman, M., Newhall, A.E.: Internal Tidal Modal Ray Refraction and Energy Ducting in Baroclinic Gulf Stream Currents, *Journal of Physical Oceanography*, 48, 1969–1993, <https://doi.org/10.1175/JPO-D-18-0031.1>, 2018.
- 664 Egbert, G.D., Ray, R.D.: Significant dissipation of tidal energy in the deep ocean inferred from satellite altimeter data, *Nature*, 405, 775–778, <https://doi.org/10.1038/35015531>, 2000.
- Fassoni-Andrade, A.C., Durand, F., Azevedo, A., Bertin, X., Santos, L.G., Khan, J.U., Testut, L., Moreira, D.M.: Seasonal to interannual variability of the tide in the Amazon estuary, *Continental Shelf Research*, 255, 104945, <https://doi.org/10.1016/j.csr.2023.104945>, 2023.
- 668 Gabioux, M., Vinzon, S.B., Paiva, A.M.: Tidal propagation over fluid mud layers on the Amazon shelf, *Continental Shelf Research*, 25, 113–125, <https://doi.org/10.1016/j.csr.2004.09.001>, 2005.
- Holloway, P.E., Merrifield, M.A.: On the Spring-Neap variability and age of the internal tide at the Hawaiian Ridge, *Journal of Geophysical Research: Oceans*, 108, <https://doi.org/10.1029/2002JC001486>, 2003.
- 672 Iwasaki, S., Isobe, A., Miyao, Y.: Fortnightly atmospheric tides forced by Spring and Neap tides in coastal waters, *Sci Rep*, 5, 10167, <https://doi.org/10.1038/srep10167>, 2015.
- Jithin, A.K., Francis, P.A.: Role of internal tide mixing in keeping the deep Andaman Sea warmer than the Bay of Bengal, *Sci Rep*, 10, 11982, <https://doi.org/10.1038/s41598-020-68708-6>, 2020.
- 676 Katavouta, A., Polton, J.A., Harle, J.D., Holt, J.T.: Effect of Tides on the Indonesian Seas Circulation and Their Role on the Volume, Heat and Salt Transports of the Indonesian Throughflow, *Journal of Geophysical Research: Oceans*, 127, e2022JC018524, <https://doi.org/10.1029/2022JC018524>, 2022.



- 680 Keckhut, P., Lefebvre, T., Hauchecorne, A., Meftah, M., Khaykin, S.: Detection of Migrating and Non-Migrating Atmospheric Tides Derived from ERA5 Temperature Meteorological analyzes, *Atmosphere*, 14(5), 895, <https://doi.org/10.3390/atmos14050895>, 2023.
- 684 Koch-Larrouy, A., Lengaigne, M., Terray, P., Madec, G., Masson, S.: Tidal mixing in the Indonesian Seas and its effect on the tropical climate system, *Clim Dyn*, 34, 891–904, <https://doi.org/10.1007/s00382-009-0642-4>, 2010.
- Koch-Larrouy, A., Madec, G., Bouruet-Aubertot, P., Gerkema, T., Bessières, L., Molcard, R.: On the transformation of Pacific Water into Indonesian Throughflow Water by internal tidal mixing, *Geophysical Research Letters*, 34, <https://doi.org/10.1029/2006GL028405>, 2007.
- 688 Kouogang, F., Koch-Larrouy, A., Carton, X., and Araujo, M.: Vertical Mode and Cyclonic Eddy Encounters Govern Internal Tides Propagation and Intermodal Cascades: High-resolution Eddy Permitting Simulations, *EGUsphere*(preprint), <https://doi.org/10.5194/egusphere-2025-6390>, 2025.
- 692 Kouogang, F., Koch-Larrouy, A., Magalhaes, J., Costa Da Silva, A., Kerhervé, D., Bertrand, A., Cervelli, E., Assene, F., Ternon, J.-F., Rousselot, P., Lee, J., Rollnic, M., and Araujo, M.: Turbulent dissipation from AMAZOMIX off the Amazon shelf along internal tide paths, *Ocean Sci.*, 21, 1589–1608, <https://doi.org/10.5194/os-21-1589-2025>, 2025.
- 696 Li, Y., Curchitser, E.N., Wang, J., Peng, S.: Tidal Effects on the Surface Water Cooling Northeast of Hainan Island, South China Sea, *Journal of Geophysical Research: Oceans*, 125, e2019JC016016, <https://doi.org/10.1029/2019JC016016>, 2020.
- Lyard, F.H., Allain, D.J., Cancet, M., Carrère, L., Picot, N.: FES2014 global ocean tide atlas: design and performance, *Ocean Science*, 17, 615–649, <https://doi.org/10.5194/os-17-615-2021>, 2021.
- 700 Martínez-Díaz-de-León, A., Castro, R., Santamaria-del-Ángel, E., Pacheco-Ruiz, I., Blanco-Betancourt, R.: Sea Surface Heat Fluxes and Fortnightly Modulation of the Surface Temperature within the Ballenas Channel, Gulf of California, *coas*, 29, 1400–1412, <https://doi.org/10.2112/JCOASTRES-D-12-00189.1>, 2013.
- 704 Munk, W., Wunsch, C.: Abyssal recipes II: energetics of tidal and wind mixing, *Deep Sea Research Part I: Oceanographic Research Papers*, 45, 1977–2010, [https://doi.org/10.1016/S0967-0637\(98\)00070-3](https://doi.org/10.1016/S0967-0637(98)00070-3), 1998.
- 708 Nagai, T., Hibiya, T.: Internal tides and associated vertical mixing in the Indonesian Archipelago, *Journal of Geophysical Research: Oceans*, 120, 3373–3390, <https://doi.org/10.1002/2014JC010592>, 2015.
- Niwa, Y., Hibiya, T.: Estimation of baroclinic tide energy available for deep ocean mixing based on three-dimensional global numerical simulations, *J Oceanogr*, 67, 493–502, <https://doi.org/10.1007/s10872-011-0052-1>, 2011.
- 712 Nugroho, D., Koch-Larrouy, A., Gaspar, P., Lyard, F., Reffray, G., Tranchant, B.: Modelling explicit tides in the Indonesian seas: An important process for surface sea water properties, *Marine Pollution Bulletin*, Special Issue: Indonesia seas management 131, 7–18. <https://doi.org/10.1016/j.marpolbul.2017.06.033>, 2018.
- 716 Pineda, J., López, M.: Temperature, stratification and barnacle larval settlement in two Californian sites, *Continental Shelf Research*, 22, 1183–1198, [https://doi.org/10.1016/S0278-4343\(01\)00098-X](https://doi.org/10.1016/S0278-4343(01)00098-X), 2002.
- Ponte, A.L., Klein, P.: Incoherent signature of internal tides on sea level in idealized numerical simulations, *Geophysical Research Letters*, 42, 1520–1526, <https://doi.org/10.1002/2014GL062583>, 2015.
- 720 Pugh, D., Woodworth, P.L.: *Sea-Level Science: Understanding Tides, Surges, Tsunamis and Mean Sea-Level Changes*, Cambridge University Press, 2014.
- Purwandana, A., Cuypers, Y., Bouruet-Aubertot, P.: Observation of internal tides, nonlinear internal waves and mixing in the Lombok Strait, Indonesia, *Continental Shelf Research*, 216, 104358, <https://doi.org/10.1016/j.csr.2021.104358>, 2021.
- 724 Ray, R.D., Susanto, R.D.: Tidal mixing signatures in the Indonesian seas from high-resolution sea surface temperature data, *Geophysical Research Letters*, vol. 43(15), 8115 – 8123, <https://doi.org/10.1002/2016GL069485>, 2016.
- 728 Ray, R.D., Susanto, R.D.: A fortnightly atmospheric ‘tide’ at Bali caused by oceanic tidal mixing in Lombok Strait, *Geoscience Letters*, 6, 6, <https://doi.org/10.1186/s40562-019-0135-1>, 2019.
- Ruault, V., Jouanno, J., Durand, F., Chanut, J., Benshila, R. Role of the Tide on the Structure of the Amazon Plume: A Numerical Modeling Approach, *Journal of Geophysical Research: Oceans*, 125, e2019JC015495, <https://doi.org/10.1029/2019JC015495>, 2020.
- 732 Sharples, J., Tweddle, J.F., Green, J.A.M., Palmer, M.R., Kim, Y.-N., Hickman, A.E., Holligan, P.M., Moore, C.M., Rippeth, T.P., Simpson, J.H., Krivtsov, V.: Spring-Neap modulation of internal tide mixing and vertical nitrate fluxes at a shelf edge in summer, *Limnology and Oceanography*, 52, 1735–1747, <https://doi.org/10.4319/lo.2007.52.5.1735>, 2007.
- 736



- Shi, W., Wang, M., Jiang, L.: Spring-Neap tidal effects on satellite ocean color observations in the Bohai Sea, Yellow Sea, and East China Sea, *Journal of Geophysical Research: Oceans*, 116, <https://doi.org/10.1029/2011JC007234>, 2011.
- 740 Smith, K.A., Rocheleau, G., Merrifield, M.A., Jaramillo, S., Pawlak, G.: Temperature variability caused by internal tides in the coral reef ecosystem of Hanauma bay, Hawai'i, *Continental Shelf Research*, 116, 1–12, <https://doi.org/10.1016/j.csr.2016.01.004>, 2016.
- 744 Souza, A.J., Pineda, J.: Tidal mixing modulation of sea-surface temperature and diatom abundance in Southern California, *Continental Shelf Research*, 21, 651–666, [https://doi.org/10.1016/S0278-4343\(00\)00105-9](https://doi.org/10.1016/S0278-4343(00)00105-9), 2001.
- 748 Sprintall, J., Gordon, A.L., Koch-Larrouy, A., Lee, T., Potemra, J.T., Pujiana, K., Wijffels, S.E.: The Indonesian seas and their role in the coupled ocean–climate system, *Nature Geosci.*, 7, 487–492, <https://doi.org/10.1038/ngeo2188>, 2014.
- Stabeno, P.J., Kachel, D.G., Kachel, N.B., Sullivan, M.E.: Observations from moorings in the Aleutian Passes: temperature, salinity and transport, *Fisheries Oceanography*, 14, 39–54, <https://doi.org/10.1111/j.1365-2419.2005.00362.x>, 2005.
- 752 Susanto, R.D., Pan, J., Devlin, A.T.: Tidal Mixing Signatures in the Hong Kong Coastal Waters from Satellite-Derived Sea Surface Temperature, *Remote Sensing*, 11, 5, <https://doi.org/10.3390/rs11010005>, 2019.
- Susanto, R.D., Ray, R.D.: Seasonal and Interannual Variability of Tidal Mixing Signatures in Indonesian Seas from High-Resolution Sea Surface Temperature, *Remote Sensing*, 14, 1934, <https://doi.org/10.3390/rs14081934>, 2022.
- 756 Tchilibou, M., Koch-Larrouy, A., Barbot, S., Lyard, F., Morel, Y., Jouanno, J., Morrow, R.: Internal tides off the Amazon shelf during two contrasted seasons: interactions with background circulation and SSH imprints, *Ocean Science*, 18, 1591–1618, <https://doi.org/10.5194/os-18-1591-2022>, 2022.
- 760 van Haren, H., Cimadoribus, A.A., Cyr, F., Gostiaux, L.: Insights from 3-D temperature sensors mooring on stratified ocean turbulence, *Geophysical Research Letters*, 43, 4483–4489, <https://doi.org/10.1002/2016GL068032>, 2016.
- 764 van Haren, H., Gostiaux, L.: High-resolution open-ocean temperature spectra: *Journal of Geophysical Research: Oceans*, 114, <https://doi.org/10.1029/2008JC004967>, 2009.
- Wentz, F. J., Gentemann, C., and Hilburn, K. A.: Remote Sensing Systems TRMM TMI, Environmental Suite on 0.25 deg grid, Version 7.1, Remote Sensing Systems, Santa Rosa, CA [data set], <https://www.remss.com/missions/tmi> (last access: 27 June 2022), 2015.
- 768 Xu, P., Yang, W., Zhu, B., Wei, H., Zhao, L., Nie, H.: Turbulent mixing and vertical nitrate flux induced by the semidiurnal internal tides in the southern Yellow Sea, *Continental Shelf Research*, 208, 104240, <https://doi.org/10.1016/j.csr.2020.104240>, 2020.
- 772 Yang, M., Khan, F.A., Tian, H., Liu, Q.: Analysis of the Monthly and Spring-Neap Tidal Variability of Satellite Chlorophyll-a and Total Suspended Matter in a Turbid Coastal Ocean Using the DINEOF Method, *Remote Sensing*, 13, 632, <https://doi.org/10.3390/rs13040632>, 2021.
- Zaron, E.D.: Mapping the nonstationary internal tide with satellite altimetry, *Journal of Geophysical Research: Oceans*, 122, 539–554, <https://doi.org/10.1002/2016JC012487>, 2017.
- 776 Zaron, E.D., Capuano, T.A., Koch-Larrouy, A.: Fortnightly variability of Chl a in the Indonesian seas, *Ocean Science*, 19, 43–55, <https://doi.org/10.5194/os-19-43-2023>, 2023.